

# Thermal conductivity of strained silicon: Molecular dynamics insight and kinetic theory approach

Cite as: J. Appl. Phys. 126, 055109 (2019); doi: 10.1063/1.5108780

Submitted: 2 May 2019 · Accepted: 9 July 2019 ·

Published Online: 1 August 2019



Vasyl Kuryliuk,<sup>1</sup>  Oleksii Nepochatyi,<sup>1</sup> Patrice Chantrenne,<sup>2</sup>  David Lacroix,<sup>3</sup>  and Mykola Isaiev<sup>1,3,a)</sup> 

## AFFILIATIONS

<sup>1</sup>Faculty of Physics, Taras Shevchenko National University of Kyiv, 64/13, Volodymrska Str., 01601 Kyiv, Ukraine

<sup>2</sup>Univ. Lyon—INSA Lyon—MATEIS—UMR CNRS 5510, F69621 Villeurbanne, France

<sup>3</sup>Université de Lorraine, CNRS, LEMTA, Nancy F-54000, France

<sup>a)</sup>Electronic mail: mykola.isaiev@univ-lorraine.fr

## ABSTRACT

In this work, we investigated the tensile and compression forces effect on the thermal conductivity of silicon. We used the equilibrium molecular dynamics approach for the evaluation of thermal conductivity considering different interatomic potentials. More specifically, we tested Stillinger-Weber, Tersoff, Environment-Dependent Interatomic Potential, and Modified Embedded Atom Method potentials for the description of silicon atom motion under different strain and temperature conditions. It was shown that the Tersoff potential gives a correct trend of the thermal conductivity with the hydrostatic strain, while other potentials fail, especially when the compression strain is applied. Additionally, we extracted phonon density of states and dispersion curves from molecular dynamics simulations. These data were used for direct calculations of the thermal conductivity considering the kinetic theory approach. Comparison of molecular dynamics and kinetic theory simulations results as a function of strain and temperature allowed us to investigate the different factors affecting the thermal conductivity of the strained silicon.

Published under license by AIP Publishing. <https://doi.org/10.1063/1.5108780>

## I. INTRODUCTION

Tuning of thermal properties of various materials is one of the key demands in material research.<sup>1–4</sup> First and foremost, such necessity arises because of continuous miniaturization of core components of various microdevices. As a result, issues related to the improvement of heat management are more and more crucial. In this context, any possibilities of increasing or lowering the thermal conductivity in semiconductor materials are very important and can encounter broad attention in several application fields.

Strain is an effective method for tuning the thermal property of various materials due to its flexibility. Strain can affect the thermal properties of a material by shifting its phonon frequencies,<sup>5,6</sup> thereby changing its heat capacity, phonon group velocities, and phonon lifetimes, all of which contribute to the lattice thermal conductivity. Many attempts have been made to study the thermal conductivity of solids under strain using experiments<sup>7–9</sup> and theoretical simulations.<sup>10–12</sup> Ross *et al.*<sup>13</sup> concluded that the thermal conductivity of semiconductors increases with the compressive strain. Picu *et al.*<sup>14</sup> studied strain effects on a model Lennard-Jones

crystal using molecular dynamics simulations. They found that the thermal conductivity increases under compression and decreases under tension. It has been observed that the thermal conductivity decreases continuously when the strain changed from compressive to tensile for bulk silicon, silicon nanowires, and silicon thin films.<sup>15</sup>

Besides, in addition to the control and the modification of material properties that can be expected, elastic stresses often arise as a result of technological processing of a crystalline solid, such as porous network formation,<sup>16,17</sup> nanostructuration,<sup>18,19</sup> amorphization,<sup>20,21</sup> and nanoinclusion.<sup>22,23</sup> Additionally, other methods of heat flux control involving phononics membranes,<sup>24</sup> dislocations,<sup>25–28</sup> and functionalization of surfaces by different coatings and shells<sup>29,30</sup> lead to the generation of strongly heterogeneous fields of elastic stresses.

For these reasons, particular emphasis on the understanding of the role of strain on thermal transport properties at the nanoscale is an urgent need. As a first step in elucidating this issue, one needs more physical insight regarding phonon transport in strained materials, and silicon is a good starting point to link theory and

experimentation. Silicon is a material of choice in today's micro- and nanoelectronics. Particularly, strained silicon is one of the best candidates for the implementation in metal oxide semiconductor devices<sup>31</sup> because of the possibility of bandgap tuning with strain. Furthermore, recent studies revealed mechanical-field control of electron spin qubits of donor impurities in silicon,<sup>32</sup> which open possibilities of strained silicon applications in spin-based quantum technologies.<sup>33</sup> The change of vibration states of silicon is also an appropriate way to tune its thermal properties.

Molecular dynamics (MD) is an important tool for predicting the thermal properties of bulk semiconductors and nanostructures, including silicon. The accuracy of the results delivered by MD simulations depends critically on the reliability of interatomic potentials. Several semiempirical potentials have been developed for Si. The most popular Si potentials were proposed by Stillinger and Weber (SW)<sup>34</sup> and Tersoff.<sup>35</sup> Other Si potential formats include the Environment-Dependent Interatomic Potential (EDIP)<sup>36</sup> and the Modified Embedded Atom Method (MEAM)<sup>37</sup> potentials. These original potentials were modified by many authors by slightly changing the analytical functions and improving the parametrization.<sup>38–42</sup> Several studies have been conducted to compare different empirical interatomic potentials for heat transport modeling in silicon;<sup>43–45</sup> however, no study has systematically compared potentials regarding the strain effect on the thermal conductivity of bulk silicon. Therefore, the first goal of this work is to test Tersoff III,<sup>38–40</sup> SW,<sup>34</sup> EDIP,<sup>36</sup> and Second Nearest Neighbour (2NN) MEAM<sup>41,42</sup> potentials for their ability to predict the thermal conductivity of silicon under hydrostatic compressive and tensile strains. Interatomic parameters of each considered potential are provided in Appendix A.

In this study, we used the equilibrium molecular dynamics (EMD) approach for the simulation of the thermal conductivity of the strained silicon. Since the thermal conductivity evaluated with molecular dynamics is sensitive to the interatomic interactions,<sup>43–45</sup> we chose the optimum potential for the simulation of the thermal conductivity of the strained Si silicon. With the chosen potential, we calculated dispersion curves, density of states, and phonon lifetimes for different temperatures and strains. However, the significant drawback of MD simulations is the classical description, which induces no energy quantization. Therefore, we additionally applied an analytic approach based on the kinetic theory (KT) of gases<sup>46</sup> for the evaluation of the thermal conductivity with the input data calculated by molecular dynamics. Finally, we investigated correlations between the temperature dependence of the thermal conductivity revealed by KT simulations with the data obtained by EMD.

## II. SIMULATION METHODS

### A. Formation of strained silicon and elastic property calculations

All MD simulations were carried out with Large-scale Atomic/Molecular Massively Parallel Simulator (LAMMPS).<sup>75</sup> The initial system was set as a single crystal silicon with a diamond lattice structure. The initial lattice parameter was set to be equal to 5.43 Å. The  $x$ ,  $y$ , and  $z$  dimensions of the silicon slab and the simulation domain were set to be equal to 10 lattice cells. It has been shown that with these cell sizes, the system-size effects can be eliminated.<sup>47,48</sup>

Additionally, we tested the impact of the simulations domain size on the strain-stress curves and found it insignificant (see Appendix B). The periodic boundary conditions were used in all directions to simulate a bulk crystal. The system was equilibrated under temperature  $T$  in the Nosé-Hoover thermostat with the use of the isotherm-isobaric (NPT) ensemble during 100 ps with a time step equal to 1 fs to achieve the equilibrium lattice parameter for each temperature and potential for the case of external pressure absence ( $P = 0$  Pa). The initial systems after equilibrium were used for thermal conductivity calculations of pristine Si structures.

Then, the pristine systems were slowly hydrostatically deformed in compression or tension. The rate of strain was set to be equal to  $10^{-3}$  ps<sup>-1</sup>. After each 0.1 ps of the deformation procedure, the information regarding strain and induced stress in the system was collected. Such a deformation was performed during 200 ps, and the final deformation was equal to  $\pm 20\%$  to achieve stress-strain curve visualization. Additionally, for the strains equal to  $\pm 1\%$ ,  $\pm 2\%$ ,  $\pm 3\%$ ,  $\pm 4\%$ , and  $\pm 5\%$ , the restart files with atom's positions and velocities were collected. These files were used for further thermal conductivity evaluation.

Figure 1 depicts the typical strain-stress curves of a silicon sample in compression/tensile tests for the four considered potentials at 300 K. As one can see from the figure, bulk modulus ( $B$ ) can be estimated from the slope of a curve divided on 3 in the elastic deformation range (blue window in Fig. 1). For all potentials,  $B$  values are the same and are equal to  $B = 100 \pm 8$  GPa. The latter value matches well with the experimental data.<sup>49,50</sup> High frequency oscillations on strain-stress curves at large tensile deformations are related to the material fracture. The abrupt changes of strain-stress curves obtained with Tersoff III and 2NN MEAM potentials at high compressive strain are caused by phase transformation in silicon under hydrostatic pressure.<sup>51,52</sup>

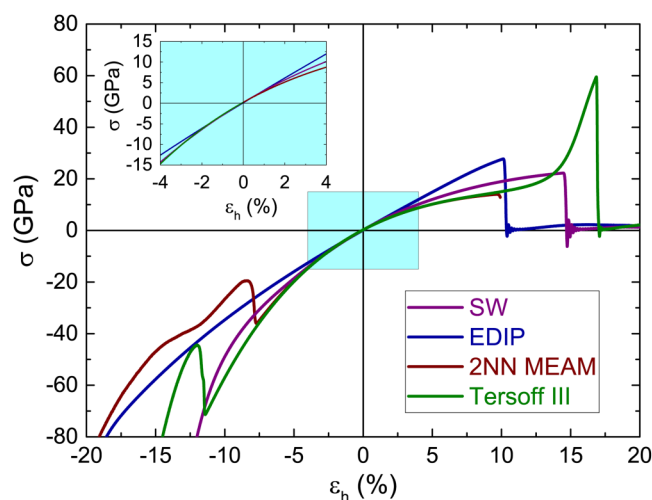


**FIG. 1.** Strain-stress curves calculated for different potentials, EDIP, Tersoff III, and 2NN MEAM at 300 K, where the negative strain stands for compression and positive for tension.

## B. Thermal conductivity evaluation

For the thermal conductivity evaluation, we used the Equilibrium Molecular Dynamics (EMD) approach, which is based on the Green-Kubo formalism. In this framework, the thermal conductivity can be evaluated from the autocorrelation of heat flux as follows:<sup>53</sup>

$$\kappa_{ij} = \frac{1}{Vk_B T^2} \int_0^\infty dt \langle J_i(t) J_j(0) \rangle, \quad (1)$$

where  $V$  is the volume of the system,  $k_B$  is Boltzmann's constant, and  $\langle J_i(t) J_j(0) \rangle$  is the heat current autocorrelation function. In general, the conductivity is averaged across all three directions to obtain the scalar conductivity.

Since EMD is based on numerical simulations, the integration time as well as the averaging time in Eq. (1) were limited to finite values. Additionally, the thermal conductivity was averaged in different directions. Thus, Eq. (1) was used in the following form:

$$\kappa = \frac{1}{3Vk_B T^2} \int_0^{t_c} dt \langle \mathbf{J}(t) \mathbf{J}(0) \rangle_t, \quad (2)$$

where  $\mathbf{J}$  is the heat flux vector,  $t_c$  is a finite correlation time for which the integration is carried out, and  $t_s$  is the sampling time over which the autocorrelation function is accumulated for averaging.

The atom structure input files of EMD calculations of pristine and strained samples are the ones described above. For thermal conductivity calculations, the systems were equilibrated again according to the Nosé-Hoover thermostat during 1 ns, but with the use of the canonical (NVT) ensemble. After equilibrium, we performed NVE integration during 25 ns. During this integration, the heat fluxes in different directions were collected and recorded. Thermal conductivities were extracted with Eq. (2). The correlation time was chosen to be equal to 10 ps, and the sampling time was 50 ps. It should be noted that we also tested the sampling time equal to 100 ps to check the stability of calculations. In this case, the duration of the NVE integration was equal to 100 ns. Particularly, the thermal conductivity for the Tersoff potential under 300 K with a longer sampling time (100 ps) was found to be equal to  $\kappa = 229 \pm 8$  W/(mK) and for a shorter sampling time (50 ps) as  $\kappa = 222 \pm 8$  W/(mK). Thus, both values are in good agreement, and, therefore, for further calculations, we used only the shorter sampling time equal to 50 ps. Since the thermal conductivity calculated based on the Green-Kubo formalism is sensitive to initial conditions, the simulations were carried for 10 different seeds. The final value of the thermal conductivity for each potential, strain and temperature was averaged among these seeds.

## C. Calculation of phonon dispersion and density of states

To get more details about the strain effect on the silicon thermal conductivity, the phonon density of states (DOS) and the phonon dispersions of silicon were calculated. Those calculations were performed using the FixPhonon module of LAMMPS. With this tool, dispersion curves can be obtained from Green's function

formalism.<sup>54,55</sup> In the latter, we consider the lattice vibrations at finite temperature  $T$ ; the  $k$ th basis atoms in the  $l$ th unit cell are displaced from their equilibrium positions  $\mathbf{r}_{lk}$  by an amount of  $\mathbf{u}_{lk}$  (atom displacement). In the reciprocal space, the displacements are obtained from the Fourier transformation of the real space ones<sup>55</sup> according to

$$\tilde{\mathbf{u}}_{k\alpha}(\mathbf{q}) = \frac{1}{\sqrt{N_{UC}}} \sum_l \mathbf{u}_{lk\alpha} e^{-i\mathbf{q}\mathbf{r}_l}, \quad (3)$$

where  $N_{UC}$  is the total number of unit cells in the crystal,  $\mathbf{r}_l$  is the equilibrium positions of  $l$ th unit cell,  $\alpha$  is the component of the atomic displacement of the  $k$ th atom in Cartesian coordinates, and  $\mathbf{q}$  is the wave vector. Green's function in the reciprocal space is given by

$$\tilde{\mathbf{G}}_{k\alpha,k'\beta}(\mathbf{q}) = \langle \tilde{\mathbf{u}}_{k\alpha}(\mathbf{q}) \tilde{\mathbf{u}}_{k'\beta}^*(\mathbf{q}) \rangle, \quad (4)$$

where the superscript  $*$  denotes the complex conjugate and  $\langle \dots \rangle$  denotes the ensemble average. With Green's function method, the dynamical matrix can be expressed as

$$\mathbf{D}_{k\alpha,k'\beta}(\mathbf{q}) = \frac{k_B T}{M} [\tilde{\mathbf{G}}^{-1}(\mathbf{q})]_{k\alpha,k'\beta}. \quad (5)$$

Here,  $M$  is the mass of the Si atom. By solving the eigenvalues of dynamical matrix  $\mathbf{D}$ , we can get the frequencies of all phonon modes as

$$|\mathbf{D}_{k\alpha,k'\beta}(\mathbf{q}) - \delta_{\alpha\beta} \delta_{kk'} \omega^2(\mathbf{q})| = 0, \quad (6)$$

where  $\omega$  is the phonon frequency. Hence, the relations between  $\mathbf{q}$  and  $\omega$  are obtained. The phonon DOS curve is computed from the phonon dispersion by dividing the frequency range into many small segments and counting the number of states in each segment.

In this work, the dynamic matrix calculations were performed in the NVE ensemble with a Langevin thermostat. The systems were equilibrated for  $0.5 \cdot 10^6$  time steps, and then the system is run in the NVE ensemble for  $6 \cdot 10^6$  time steps to record the atomic displacements and velocities. Using the eigenvalues of the dynamical matrices, the phonon DOS and the phonon dispersions were then calculated using the auxiliary postprocessing code *phana*.<sup>55</sup>

## D. Calculation of phonon relaxation times

The vibrational lifetime was estimated from the recently developed method based on the Monte Carlo-based moment approximation.<sup>56–58</sup> Beginning with the harmonic force constant matrix, the normal modes are found, indexed by wave vector  $q$  and branch  $b$ . The calculation involves ensemble averaging of products of normal mode amplitudes  $A_b$  and accelerations  $\dot{A}_b$ , which are obtained by projecting the atomic displacements and forces onto the normal modes. The mode lifetimes are obtained from<sup>59</sup>

$$\tau_q = \frac{1.41}{\sqrt{\frac{\langle A_q \dot{A}_q \rangle}{\langle A_q^2 \rangle} \left( \frac{\langle \dot{A}_q^2 \rangle \langle A_q^2 \rangle}{\langle A_q \dot{A}_q \rangle^2} - 1 \right)}}. \quad (7)$$

Calculations of phonon relaxation times were carried out with *Jazz* python wrapper for LAMMPS,<sup>59,60</sup> implemented to calculate the lifetimes of vibrational normal modes.

### III. ELEMENTARY KINETIC THEORY APPROACH FOR PHONON PROPAGATION

#### A. Thermal conductivity evaluation

In this section, we will describe elements of the kinetic theory approach for phonon propagation to calculate the thermal conductivity of strained Si. For the calculation, we use the analytical model developed previously by Chantrenne *et al.*<sup>46</sup> The model considers phonons to be particles that follow Bose-Einstein statistics. The thermal conductivity  $\kappa$  in the direction  $z$  associated with the phonons  $(q, p)$  can be written as

$$\kappa_z(q, p) = C(q, p)v^2(q, p)\tau(q, p)\cos^2[\theta_z(q)], \quad (8)$$

where  $q$  is the wave vector,  $p$  is its polarization, and  $v$  is the group velocity determined from the dispersion curves,

$$v = \frac{d\omega(q, p)}{dq}, \quad (9)$$

with  $v$  being the angular velocity,  $\tau(q, p)$  being the phonon relaxation time due to the phonon-scattering phenomena,  $\theta_z(q)$  being the angle between the wave vector  $q$  and the direction  $z$ , and  $C(q, p)$  being the specific heat per unit volume,

$$C(q, p) = k_B x^2 \frac{e^x}{V(e^x - 1)^2}, \quad (10)$$

$$x = \frac{\hbar\omega(q, p)}{k_B T}. \quad (11)$$

The total thermal conductivity is the sum of the individual contributions due to all the wave vectors  $q$  and polarizations  $p$ ,

$$\kappa_z = \sum_q \sum_p \kappa_z(q, p). \quad (12)$$

In our case, the system is isotropic and its size can be considered infinite. Thus, the sum in Eq. (12) becomes an integral. It is expressed in terms of the angular frequency

$$\begin{aligned} \kappa &= 6 \frac{k_B}{3 \frac{a^3}{4}} \int_0^\infty d\omega \left( \frac{\hbar\omega}{k_B T} \right)^2 \frac{e^{\frac{\hbar\omega}{k_B T}}}{(e^{\frac{\hbar\omega}{k_B T}} - 1)^2} D(\omega) \\ &\quad \times \sum_p \xi(\omega, p) v^2(\omega, p) \tau(\omega, p), \end{aligned} \quad (13)$$

where 6 is the number of polarizations,  $\frac{a^3}{4}$  is the volume of a primitive cell,  $D(\omega)$  is the phonon density of states ( $\int_0^\infty D(\omega) d\omega = 1$ ),  $\tau(\omega, p)$  is the phonon relaxation time,  $\xi(\omega, p)$  are coefficients, that

express the contributions of different polarizations to DOS,

$$\begin{aligned} \xi(\omega, p) &\propto \frac{q^2(\omega, p)}{v(\omega, p)}, \\ \sum_p \xi(\omega, p) &= 1. \end{aligned} \quad (14)$$

#### B. Relaxation times

In order to theoretically assess the thermal conductivity, the last needed parameter is the phonon relaxation time. In general, several scattering mechanisms are at play. According to the Mathiessen rule, the resulting relaxation time (RT) is

$$\tau^{-1}(\omega, p) = \tau_U^{-1}(\omega, p) + \tau_{BC}^{-1}(\omega, p) + \tau_d^{-1}(\omega, p), \quad (15)$$

where  $\tau_U^{-1}(\omega, p)$  is RT due to Umklapp scattering,  $\tau_{BC}^{-1}(\omega, p)$  is RT due to the presence of system boundaries, and  $\tau_d^{-1}(\omega, p)$  is RT due to defect or impurity scattering. In our case, the system is considered infinite (periodic boundary conditions set in EMD), so  $\tau_{BC}^{-1}(\omega, p) = 0$ , and the lattice is supposed to be perfect, so it has no defects. Thus,

$$\begin{aligned} \tau^{-1}(\omega, p) &= \tau_U^{-1}(\omega, p) \\ &= \begin{cases} A_T \omega^{\chi_T} T^{\xi_T} \exp\left(\frac{B_T}{T}\right) & \text{TA branches,} \\ A_L \omega^{\chi_L} T^{\xi_L} \exp\left(\frac{B_L}{T}\right) & \text{LA branches.} \end{cases} \end{aligned} \quad (16)$$

Besides, it should be mentioned that the implemented approach for calculations of relaxation times only gives a global relaxation time. Decomposition of different contributions is a challenging issue and is not the purpose of this work. Therefore, we fitted numerical data evaluated with Eq. (7) by the following equation for all polarizations:

$$\tau(\omega, p) = A^{-1} \omega^{-\chi} T^{-\xi} \exp(-B/T). \quad (17)$$

The fitting was performed to overcome issues arising because of the significant scattering of data evaluated by MD (see Fig. 6). The fitting parameters are presented in Appendix C (Table V).

### IV. RESULTS AND DISCUSSION

In this section, the results of calculations of the thermal conductivity  $\kappa$  of Si under hydrostatic strain  $\epsilon_h$  using SW, EDIP, 2NN MEAM, and Tersoff III potentials at  $T = 300$  K will be discussed. The strain-dependencies of the thermal conductivity predicted with the use of these potentials are plotted in Fig. 2. First, it should be noted that the thermal conductivity evaluated with MD simulations overestimates the experimental results for natural<sup>61</sup> and highly isotopically enriched<sup>62</sup> Si [ $\kappa = 130$ – $160$  W/(m K) for 300 K]. As discussed previously, MD is based on classical laws of motion and quantum phenomena are not taken into account. This behavior is well known; however, in further analysis, we will only focus on the dependence of the thermal conductivity vs applied strain as a main parameter for the chosen potential reliability.

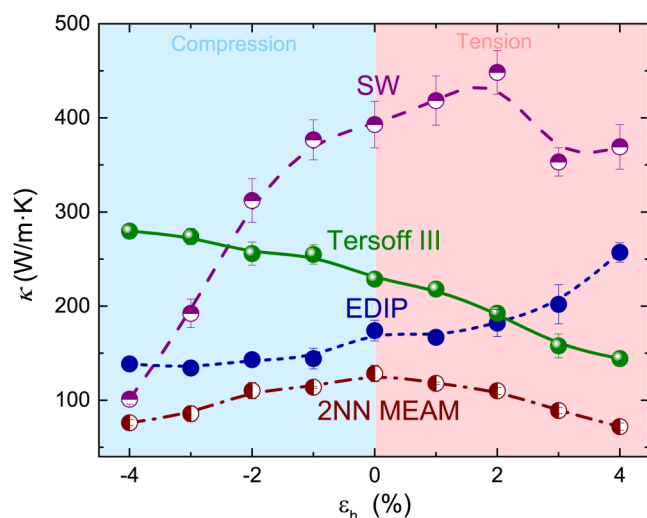


**FIG. 2.** Thermal conductivity of silicon as a function of hydrostatic strain for SW potential, EDIP, Tersoff III, and 2NN MEAM at 300 K.

Figure 2 shows that the calculated thermal conductivity of the unstrained SW silicon is about 393 W/(m K). Under compression strain, the thermal conductivity of SW silicon rapidly decreases, which contradicts previously published MD simulation results for bulk silicon<sup>15</sup> and bulk argon.<sup>14</sup> For a tensile strain, the SW potential leads to nonmonotonic dependence of the thermal conductivity, which is not in agreement with other data already revealed by the MD method.<sup>14,15</sup> Therefore, the use of such potentials is clearly inappropriate for the simulation of the thermal conductivity of silicon under hydrostatic strain.

Next, the value of  $\kappa$  resulting from the EDIP calculations for the unstrained silicon was found to be about 174 W/(m K). This potential gives also nonphysical trends  $\kappa(\epsilon_h)$ : the thermal conductivity increases continuously from compression strain to tensile hydrostatic strain, which is in a sharp contrast to the expected dependence.

Despite 2NN MEAM potential (see Fig. 2) giving a correct strain dependence of  $\kappa$  with the increase of the tensile strain, it gives an insignificant increase with the increase of compression strain. Therefore, the 2NN MEAM potentials may not be suitable for studying the strain effect on the thermal conductivity of silicon.

Finally, the calculated value of  $\kappa$  for the unstrained silicon with the Tersoff III potential is about 229 W/(m K). This is in good agreement with other MD results.<sup>63</sup> It can be noticed that the thermal conductivity of Tersoff silicon decreases continuously when the applied strain is changed from compressive to tensile. For a 4% tensile hydrostatic strain, there is a 37% reduction [from 229 W/(m K) to 144 W/(m K)] in the thermal conductivity. On the other side, at a 4% compressive hydrostatic strain, the thermal conductivity increases 22% to 280 W/(m K). This result qualitatively corresponds to the experimental data obtained by Andersson and Backstrom<sup>7</sup> for the thermal conductivity of silicon under hydrostatic pressure. According to their experiments, the thermal

conductivity  $\kappa(P)$  slowly increases at room temperature with hydrostatic pressure  $P$  as  $\kappa/\kappa_0 = 1 + 0.004P$ , where  $\kappa_0$  is the thermal conductivity of the unstrained silicon and  $P$  being measured in GPa. From Fig. 1, the strain of  $-4\%$  corresponds to the hydrostatic pressure of about 15 GPa. Therefore, the expected increase of the thermal conductivity according to this equation would be equal to 6%, which is smaller than the one calculated with the Tersoff potential. More importantly, we notice that the general trend of  $\kappa(\epsilon_h)$  variations obtained with the Tersoff III potential, plotted in Fig. 2, is similar to the previously reported strain effects on the thermal conductivity of bulk silicon<sup>7,11,15</sup> and Si nanostructures.<sup>64,65</sup>

The results shown in Fig. 2 indicate that only Tersoff III potential is reliable for thermal conductivity calculations of Si under hydrostatic strain, while SW, EDIP, and 2NN MEAM empirical potentials fail in comparison with experimental<sup>7</sup> and DFT results,<sup>12</sup> especially for compressive strain. Such a mismatch arises because these potentials were parametrized to reproduce physical properties of some stable structures of silicon. Thus, these potentials could not describe correctly the phase transformation considering the latter specific parametrization. Silicon undergoes a phase change from the diamond lattice structure to the  $\beta$ -Sn lattice structure at  $T = 300$  K, when compressive stress becomes greater than 12 GPa.<sup>52</sup> This transition, using MD and Tersoff potential, is observed for a larger pressure (60 GPa)<sup>51</sup> than the one experimentally measured.

The first possible explanation for the differences between the potentials in predicting the  $\kappa(\epsilon_h)$  dependencies of silicon under hydrostatic compression is the wide range of cutoff radius  $r_c$  of each potential. The corresponding value  $r_c$  is 3.77 Å for the SW potential, 3.12 Å for the EDIP potential, 4.3 Å for the 2NN MEAM potential, and 3.0 Å for the Tersoff III potential. Since these empirical potentials are optimized for a particular local environment of atomic configurations, they are generally not designed for conditions where the number of interacting neighbors can change abruptly. In fact, when the atomic structure is strongly compressed, whose number of neighboring atoms taken into account in the energy calculation may drastically change, leading to sharp energy variations. The fact that the Tersoff III potential is applicable over a relatively wide range of compressive strain is due to its short cutoff range.

Additionally, different functional forms and the number of fitted parameters also lead to various thermal conductivity behavior when modifying the strain. For example, the SW potential is a linear combination of two- and three-body interaction terms that stabilize the diamond cubic structure of the crystalline silicon. It has only eight independent parameters and it is fitted to reproduce few experimental properties of both crystallized and liquid silicon. The Tersoff III functional form includes many-body interactions, thanks to a bond order term. This potential has 13 adjustable parameters, which are determined by the heat of formation, cohesive energy, bulk modulus, and the relative stability of various Si polytypes obtained from calculations and experiments. The EDIP potential has a functional form similar to that of Tersoff but slightly more complicated. Thirteen parameters are determined by fitting to a fairly small *ab initio* database. MEAM is an angle dependent functional form that evolved out of the simpler



embedded atom method. Because parameter values of Tersoff III potential were determined by fitting the elastic constants,<sup>38</sup> the potential is more likely to be applicable for the analysis of deformation behavior. The latter suggests that the Tersoff III potential would be a reliable choice for describing Si thermal transport properties under hydrostatic strain. So, further consideration of this work will be carried out with this empirical potential.

Figure 3 shows the calculated thermal conductivity of bulk Si crystal with the use of the Tersoff III potential under hydrostatic compressive and tensile strains at the temperature range of 300–1100 K comparing to the results of the unstrained case. The results indicate that, for hydrostatic compression, the strain field increases the thermal conductivity and enables to affect the conductivity in the whole range of temperature from 300 to about 900 K, while the tensile hydrostatic strain decreases the thermal conductivity of silicon. For the temperatures over  $\sim 900$  K, the strain effects on the thermal conductivity become weak enough to be negligible.

Eventually, we present further analysis of the thermal conductivity variation with hydrostatic strain and temperature based on Eq. (13). From this equation, we can consider the changes in phonon density of states, phonon group velocity, and phonon relaxation time to understand the effect of hydrostatic strain on the thermal conductivity of Si. Moreover, Eq. (13) takes into account the energy distribution on the phonon mode as a function of the temperature level.

First, Fig. 4 shows the strain effect on the phonon DOS  $D(\omega)$  for bulk and strained silicon at 3% compressive and tensile strains. The calculations with the Tersoff III potential for unstrained silicon satisfactorily reproduce both the structure of the experimental dependence  $D(\omega)$  and the frequency positions of phonon modes. It is shown that the optical phonon modes show a red shift when the tensile strain is applied, while a blue shift is observed for the compressive strain. At a 3% tensile hydrostatic strain, the frequency

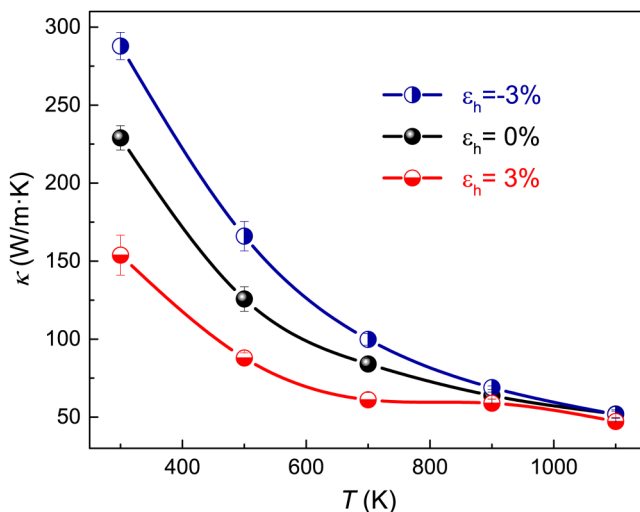


**FIG. 3.** Strain-dependent bulk thermal conductivity of silicon between 300 and 1100 K for the Tersoff III potential.

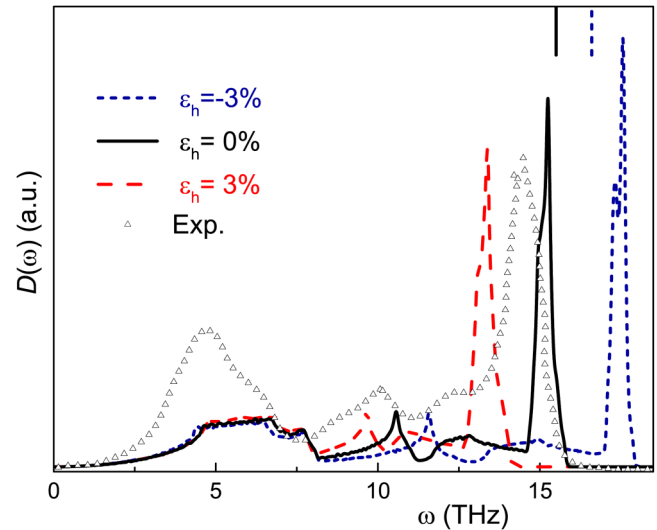


**FIG. 4.** Phonon DOS of silicon calculated with the Tersoff III potential at 300 K under different hydrostatic strains:  $-3\%$ ,  $0\%$ , and  $3\%$ . Triangles correspond to the experimental dependence  $D(\omega)$  obtained by inelastic neutron scattering.<sup>69</sup> The vertical lines at the top represent the experimental peak positions of the LO phonon mode in unstrained (solid line) and compressed at 3% (dashed line) bulk Si adopted from Ref. 66.

of the optical phonon mode changes from 15.3 to 13.4 THz ( $\Delta\omega = -1.9$  THz), while at a 3% compressive hydrostatic strain, the frequency shift is  $\Delta\omega = 2.2$  THz. The last result correlates with the experimental Raman spectra obtained by Weinstein and Piermarini<sup>66</sup> for silicon under the hydrostatic pressure. According to their experiments, the frequency  $\omega_{LO}$  of the LO phonon mode in Si shifts with pressure  $P$  as  $\omega_{LO} = 15.57 + 0.16P - 0.002P^2$  (THz). The spectral positions of the LO phonon bands obtained by using this relation for pristine and compressed at 3% silicon are shown by the straight vertical lines in Fig. 4. The expected frequency shift from the experimental data is about 1.1 THz and is smaller than the one obtained from MD simulations with the Tersoff III potential.

Consequently, optical phonons will have a lower or higher energy in comparison to the unstrained case when a strain is applied. There are similar peak shifts for longitudinal acoustic (LA) phonons, indicating that the hydrostatic strain has a significant effect on them as well. In particular, the frequency shift for LA phonons peak in DOS is  $\Delta\omega = -0.9$  THz (from 10.6 THz to 9.7 THz) and  $\Delta\omega = 1.0$  THz for 3% tensile and compressive hydrostatic strains, respectively. On the other hand, variations in transverse acoustic (TA) phonons are not significant compared to the LA and optical phonons. It is known that optical phonons contribute little to heat transfer,<sup>67,68</sup> so strain-induced transformations of phonon DOS may affect the thermal conductivity of silicon mostly due to the frequency shift of the LA phonon modes.

In addition, our calculations show that temperature has little effect on the phonon DOS (not presented in Fig. 4). For example, the frequency shift for LA phonons peak in DOS is only

$\Delta\omega = -0.3$  THz, when the temperature changes from 300 to 1100 K.

The changes in phonon group velocity can be obtained from the dispersion curves, which are plotted in Fig. 5 for the typical hydrostatic strains (−3%, 0%, and 3%). The dispersion curves for unstrained Si are compared to the experimental results, adopted from the work of Ref. 70. Tersoff III overestimates TA modes by more than 40% for all large wave vectors, which leads to a logical increase in the thermal conductivity compared to the experimental ones. As shown in Fig. 5, as the strain condition changes from compressive to tensile, transverse acoustic phonon branches change little, while the frequency of optical and longitudinal acoustic phonon branches decrease and the whole range of frequency becomes narrowed. This agrees with the change of DOS presented in Fig. 4. The decrease of the maximum phonon frequency as the strain moves from compressive to tensile leads to decreasing phonon group velocities.

The evaluated phonon group velocities are plotted in Fig. 5 by dotted line curves. As one can see, strain does not affect the TA phonon group velocity, while the LA one decreases as the applied strain is changed from compressive to tensile. These observations are consistent with our EMD thermal conductivity calculations presented above (Fig. 3). When the Si structure is under compression, LA phonon frequencies are larger as well as group velocities. It results in a larger phonon heat flux and thus in a bigger thermal conductivity as compared to the pristine case. On the contrary, the traction of Si structure reduces maximum frequencies and related group velocities and thus heat flux and thermal conductivity. In addition, our calculations show that the temperature has a negligible effect on the dispersion curves of silicon and, consequently, on the phonon velocities. This is confirmed, in Fig. 5, that the dashed lines show the calculated dispersion curves for silicon at  $T = 1100$  K. For example, our calculations show (not presented in

Fig. 5) that the increase in the temperature from 300 to 1100 K leads to changes in the group velocity only  $\Delta v \leq 2\% - 4\%$  for transverse acoustic phonons, and  $\Delta v \leq 1\%$  for longitudinal acoustic phonons in a wide range of wave vectors.

In Fig. 6, we present the frequency dependent phonon lifetimes in pristine and strained silicon at 300 K and 1100 K. As one can see, lifetime  $\tau$  varies insignificantly as the system moves from compressive to tensile hydrostatic strain. For example, the mean phonon lifetimes for LA phonons with frequency  $\omega \simeq 10$  THz are about  $\tau = 7$  ps,  $\tau = 8$  ps, and  $\tau = 6$  ps in pristine, compressed at −3% and tensed at 3% silicon, respectively. The strain-induced changes in phonon lifetimes for TA modes are also insignificant, so the reduction of the phonon mean free path as the system moves from compressive to tensile hydrostatic strain is mostly associated with the decreasing group velocities described above. Additionally, Fig. 6 shows a significant (more than three times) reduction of the phonon lifetimes over almost the whole frequency range when the temperature increases from 300 K to 1000 K. This reduction results from increasing phonon-scattering rate due to phonon-phonon interaction. Therefore, the trend shown in Fig. 3 for the temperature dependence of the thermal conductivity is mainly associated with changes in phonon lifetimes. Finally, this analysis shows that the strain and temperature dependence of the thermal conductivity of silicon arises from the change of the phonon DOS and phonon group velocity, which monotonically decreases when strain changes from compressive to tensile, and the temperature dependence of the phonon relaxation time.

The comparison of MD data calculated with the Tersoff III potential with the results of the analytical simulation can be made from Fig. 7. As one can see, there are qualitative correlations between the results of both approaches. For analytical calculations, the DOS and dispersion curves were directly taken from the MD simulations (Figs. 4 and 5, respectively), which were also performed

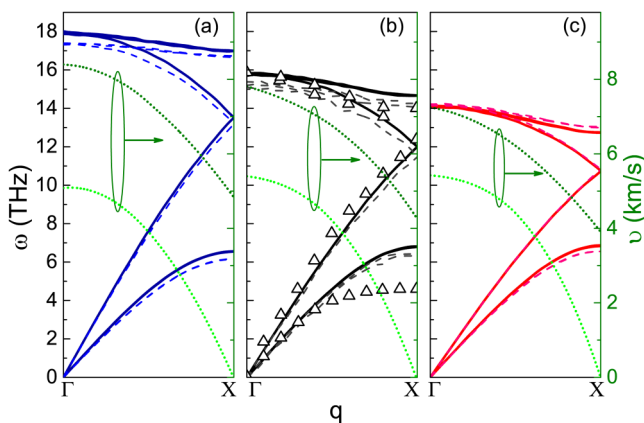


**FIG. 5.** Phonon dispersion curves of silicon calculated with the Tersoff III potential at 300 K (solid lines) and 1100 K (dashed lines) under different hydrostatic strains: (a) −3%, (b) 0%, and (c) 3%. Triangles correspond to the experimental data from Ref. 70. The dotted lines represent the phonon group velocities, obtained from the dispersion curves for longitudinal and transverse acoustic phonons.

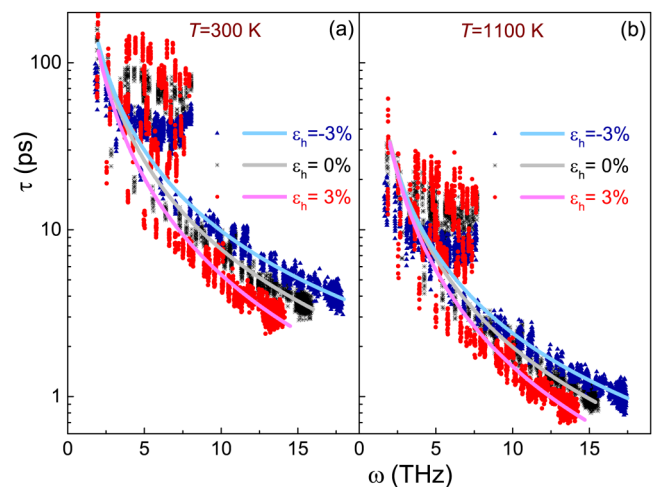


**FIG. 6.** Phonon lifetimes of silicon calculated with the Tersoff III potential at 300 K (a) and 1100 K (b) under different hydrostatic strains: −3%, 0%, and 3%. The solid lines correspond to fitting of the simulated data with Eq. (17).

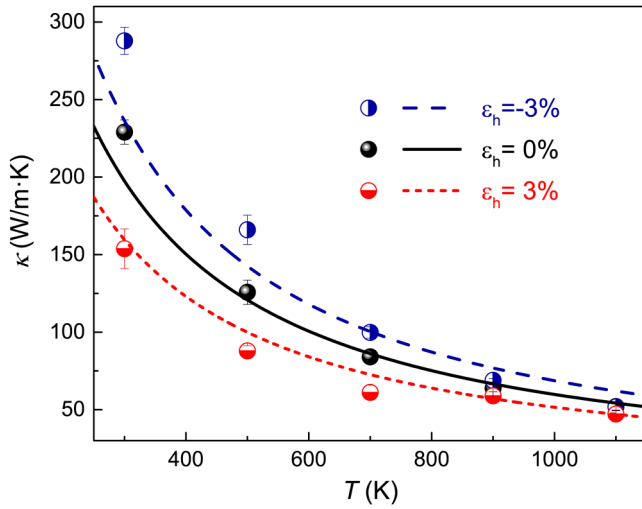


**FIG. 7.** Strain-dependent bulk thermal conductivity of silicon between 300 and 1100 K; circles: EMD simulation results; lines: kinetic theory results.

with the Tersoff III potential. The phonon lifetimes were first calculated with Eq. (7) for the Tersoff III potential, and then, because of data scattering, they were fitted with Eq. (17). The calculated lifetimes with the fitting curves are presented in Fig. 6. Fitting curves were used for analytical calculations of the thermal conductivity with the KT analytical approach.

The quantitative correlations are observed only in the temperature range from 500 to 900 K. Some mismatches in the low temperature range (below Debye temperature) can be explained by the classical nature of MD simulations; i.e., the mean number of phonons does not depend on their vibration frequency in this case. Using quantum correction (see Appendix D) mostly gives general trends. However, thermal conductivity could not be fully corrected with the latter approach.<sup>71</sup> Thus, for the low temperature range, simulation approaches based on the KT simulations are more reliable. Some mismatches occurring at higher temperatures correspond to the increasing role of higher-order inharmonic phenomena in the strained silicon, because we get close to the melting temperature.

## V. CONCLUSIONS

In this study, we considered the thermal transport in the crystalline silicon under different magnitudes of hydrostatic strains. Particularly, we considered Tersoff III, Stillinger-Weber (SW), Environment-Dependent Interatomic Potential (EDIP), and Second Nearest Neighbour (2NN) Modified Embedded Atom Method (MEAM) potentials for the thermal conductivity evaluation of the strained silicon with the use of the equilibrium molecular dynamics approach. First, the systems were created by expansion and compression of the crystalline silicon. During this step, strain-stress curves were extracted for all potentials. All potentials give a similar value of the bulk modulus (slope of the strain-stress curve).

However, only the Tersoff potential gives dependence of the thermal conductivity on the strain, which corresponds well with the experimental data. Thus, this potential was used further for the calculation of dispersion curves, density of states, and relaxation time for obtaining physical insight regarding the thermal conductivity behavior of the strained silicon.

In addition, these data were used in the analytic model based on the kinetic theory. In such a way, the dependence of the thermal conductivity on the temperature was calculated from analytical relations and correlated with the ones evaluated with the equilibrium molecular dynamics approach. Both dependencies revealed good qualitative agreement. Nevertheless, some quantitative mismatches were observed for low and high temperatures. Mismatches at low temperatures may arise because of quantum corrections (see Appendix D for more details on the latter correction). At the same time, the discrepancies for high temperatures may arise as we get close to the melting temperature.

These results bring new insights about strained silicon thermal properties. In future work, the modeling of nanostructures, which exhibits such strained areas, could be of great interest to tailor phonon transport properties.

## ACKNOWLEDGMENTS

This work has been partially funded by the French National Center for Scientific Research (CNRS) Energy unit (Cellule Energie) through the project ImHESurNaASA. We acknowledge the partial financial support of the scientific pole EMPP of the University of Lorraine. The publication contains the results obtained in the frames of the research work “Features of photothermal and photoacoustic processes in low-dimensional silicon-based semiconductor systems” (Ministry of Education and Science of Ukraine, state registration number 0118U000242). We acknowledge Dr. Vladimir Lysenko (INL, INSA Lyon) for fruitful discussions.

## APPENDIX A: POTENTIAL MODELS

### 1. Stillinger-Weber potential

The SW potential is written in the following form:<sup>34</sup>

$$U_{tot} = \sum_{i<j} \phi_2(r_{ij}) + \sum_{i<j<k} \phi_3(r_{ij}, r_{ik}, \theta_{ijk}), \quad (A1)$$

$$\phi_2 = A_{ij} \epsilon_{ij} \left[ B_{ij} \left( \frac{\sigma_{ij}}{r_{ij}} \right)^{p_{ij}} \right] e^{\frac{\sigma_{ij}}{r_{ij}^{q_{ij}-a_{ij}}}}, \quad (A2)$$

$$\phi_3 = \lambda_{ijk} \epsilon_{ijk} [\cos \theta_{ijk} - \cos \theta_{0ijk}]^2 \times e^{\frac{\gamma_{ij}\sigma_{ij}}{r_{ij}^{q_{ij}-a_{ij}}}} e^{\frac{\gamma_{ik}\sigma_{ik}}{r_{ik}^{q_{ik}-a_{ik}}}}. \quad (A3)$$

The corresponding parameters for the SW potential are provided in Table I.



**TABLE I.** Stillinger-Weber potential parameters for silicon.<sup>34</sup>

$\epsilon$ (eV)	2.1683	$\sigma$ (Å)	2.0951
$a$	1.80	$\lambda$	21.0
$\gamma$	1.20	$\cos \theta_0$	-0.333 333 333 333
$A$	7.049 556 277	$B$	0.602 224 558 4
$p$	4.0		

## 2. Environment-dependent interatomic potential

The EDIP potential is written as<sup>36</sup>

$$U_{tot} = \sum_{i<j} \phi_2(r_{ij}, Z_i) + \sum_{i<j<k} \phi_3(r_{ij}, r_{ik}, Z_i), \quad (\text{A4})$$

$$\phi_2 = A \left[ \frac{B^p}{r_{ij}} - e^{-\beta Z_i^2} \right] e^{\frac{a}{r_{ij}-a}}, \quad (\text{A5})$$

$$\phi_3 = e^{\frac{\gamma}{r_{ij}-a}} e^{\frac{\gamma}{r_{ik}-a}} h(\cos \theta_{ijk}, Z_i), \quad (\text{A6})$$

$$Z_i = \sum_{m \neq i} f(r_{im}), f(r) = \begin{cases} 1, & r < c, \\ \frac{a}{e^{1-x^3}}, & c < r < a, \\ 0, & r > a, \end{cases} \quad (\text{A7})$$

$$h(l, Z) = \lambda \left[ 1 - e^{Q(Z)(l+\tau(Z))^2} + \eta Q(Z)(l+\tau(Z))^2 \right], \quad (\text{A8})$$

$$Q = Q_0 e^{-\mu Z}, \quad \tau = u_1 + u_2(u_3 e^{-u_4 Z} - e^{-2u_4 Z}). \quad (\text{A9})$$

The corresponding parameters for the EDIP potential are provided in Table II.

## 3. Modified embedded atom method potential

In the 2NN MEAM formalism,<sup>41,42</sup> the total energy of a system is given by

$$U_{tot} = \sum_i \left[ F_i(\bar{\rho}_i) + \frac{1}{2} \sum_{j \neq i} S_{ij} \varphi_{ij}(R_{ij}) \right], \quad (\text{A10})$$

**TABLE II.** EDIP potential parameters for silicon.<sup>36</sup>

$A$ (eV)	7.982 173	$B$ (Å)	1.507 546 3
$a$ (Å)	3.121 382	$c$ (Å)	2.560 910 4
$\alpha$	3.108 384 7	$\beta$	0.007 097 5
$\eta$	0.252 324 4	$\gamma$ (Å)	1.124 794 5
$\lambda$ (eV)	1.453 310	$\mu$	0.696 632 6
$u_1$	1.124 794 5	$\sigma$ (Å)	0.577 410 8
$u_2$	1.453 310 8	$Q_0$	0.252 324 4
$u_3$	0.696 632 6	$\rho$	1.208 519 6
$u_4$	1.208 519 6		

$$F(\bar{\rho}_i) = A E_c (\bar{\rho}_i / \bar{\rho}_i^0) \ln (\bar{\rho}_i / \bar{\rho}_i^0), \quad (\text{A11})$$

$$\bar{\rho}_i = \bar{\rho}_i^{(0)} G(\Gamma), \quad (\text{A12})$$

$$G(\Gamma) = \frac{2}{1 + e^{-\Gamma}}, \quad \Gamma = \sum_{k=1}^3 t_i^{(k)} \left( \frac{\bar{\rho}_i^{(k)}}{\bar{\rho}_i^{(0)}} \right)^2, \quad (\text{A13})$$

$$(\bar{\rho}_i^{(0)})^2 = \left[ \sum_{j \neq i} \rho_j^{a(0)} \right]^2, \quad (\text{A14})$$

$$(\bar{\rho}_i^{(1)})^2 = \sum_{\alpha} \left[ \sum_{j \neq i} \frac{r_{ij}^{\alpha}}{r_{ij}} \rho_j^{a(1)} \right]^2, \quad (\text{A15})$$

$$(\bar{\rho}_i^{(2)})^2 = \sum_{\alpha, \beta} \left[ \sum_{j \neq i} \frac{r_{ij}^{\alpha} r_{ij}^{\beta}}{r_{ij}^2} \rho_j^{a(2)} \right]^2 - \frac{1}{3} \left[ \sum_{j \neq i} \rho_j^{a(2)} \right]^2, \quad (\text{A16})$$

$$(\bar{\rho}_i^{(3)})^2 = \sum_{\alpha, \beta, \gamma} \left[ \sum_{j \neq i} \frac{r_{ij}^{\alpha} r_{ij}^{\beta} r_{ij}^{\gamma}}{r_{ij}^3} \rho_j^{a(3)} \right]^2 - \frac{3}{5} \sum_{\alpha} \left[ \sum_{j \neq i} \frac{r_{ij}^{\alpha}}{r_{ij}} \rho_j^{a(3)} \right]^2, \quad (\text{A17})$$

$$\rho_i^{a(k)}(r_{ij}) = e^{-\beta_i^{(k)}(r_{ij}/r_e - 1)}, \quad (\text{A18})$$

$$E^u(r) = -E_c(1 + a^* + d(a^*)^3), \quad (\text{A19})$$

$$a^* = \alpha(r/r_e - 1), \quad (\text{A20})$$

$$\alpha = \sqrt{9B\Omega/E_c}. \quad (\text{A21})$$

The corresponding parameters for the 2NN MEAM potential are provided in Table III.

## 4. Tersoff potential

The Tersoff potential describes the atomic interaction as follows:<sup>39,40</sup>

$$U_{tot} = \sum_{i<j} f_C(r_{ij}) [f_R(r_{ij}) + b_{ij} f_A(r_{ij})], \quad (\text{A22})$$

**TABLE III.** MEAM potential parameters for silicon.<sup>72</sup>

$A$	0.58	$B$ (dyne/cm <sup>2</sup> )	$0.99 \cdot 10^{12}$
$r_e$ (Å)	2.35	$E_c$ (eV)	4.63
$\beta^{(0)}$	3.55	$t^{(0)}$	1.0
$\beta^{(1)}$	2.57	$t^{(1)}$	1.8
$\beta^{(2)}$	0.0	$t^{(2)}$	5.25
$\beta^{(3)}$	7.5	$t^{(3)}$	-2.61
$C_{\max}$	2.8	$C_{\min}$	1.41

**TABLE IV.** Tersoff potential parameters for silicon.<sup>39,40</sup>

$m$	3.0	$n$	0.787 34
$R$ (Å)	2.85	$D$ (Å)	0.15
$c$	$1.0039 \cdot 10^5$	$d$	16.217
$A$ (eV)	1830.8	$B$ (eV)	471.18
$\lambda_1$ (Å <sup>-1</sup> )	2.4799	$\beta$	$1.1 \cdot 10^{-6}$
$\lambda_2$ (Å <sup>-1</sup> )	1.7322	$\cos \theta_0$	-0.598 25
$\lambda_3$ (Å <sup>-1</sup> )	0.0		

$$f_C(r) = \begin{cases} 1, & r < R - D, \\ \frac{1}{2} - \frac{1}{2} \sin\left(\frac{\pi(r-R)}{2D}\right), & R - D < r < R + D \\ 0, & r > R + D, \end{cases} \quad (\text{A23})$$

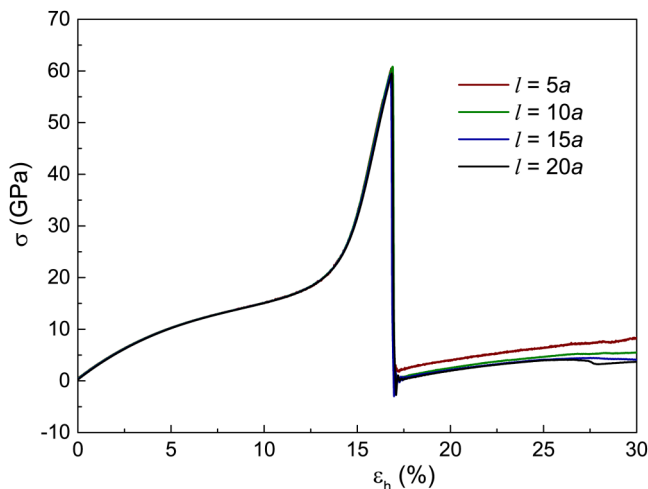
$$f_A(r) = -Be^{-\lambda_2 r}, \quad (\text{A24})$$

$$b_{ij} = \left(1 + \beta^n \zeta_{ij}^n\right)^{-\frac{1}{2n}}, \quad (\text{A25})$$

$$\zeta_{ij} = \sum_{k \neq i,j} f_C(r_{ik}) g(\theta_{ijk}) e^{\lambda_3^m (r_{ij}-r_{ik})^m}, \quad (\text{A26})$$

$$g(\theta) = 1 + \frac{c^2}{d^2} - \frac{c^2}{d^2 + (\cos \theta - \cos \theta_0)^2}. \quad (\text{A27})$$

The corresponding parameters for the Tersoff potential are provided in Table IV.

**FIG. 8.** Impact of the cell number in the simulation domain ( $l$ ) on the strain-stress curves for the Tersoff III potential.

## APPENDIX B: IMPACT OF A CELL NUMBER IN THE SIMULATION DOMAIN ON STRESS-STRAIN CURVES

The several sizes of simulation domain ( $l$ ) were checked to find appropriate ones for further simulations. As an example, Fig. 8 presented the results of simulations of stress-strain curves for Tersoff III potentials.<sup>35,39,40</sup> The situation when the simulations domain has a number of cells equal to 5, 10, 15, and 20 are demonstrated. In Fig. 8,  $a$  is the lattice parameter.

## APPENDIX C: PARAMETERS OF FITTING OF PHONON LIFETIME

Phonon lifetimes evaluated with MD [Eq. (7)] were fitted with the following equation:

$$\tau(\omega, p) = A^{-1} \omega^{-\chi} T^{-\xi} \exp(-B/T). \quad (\text{C1})$$

Parameters of the fitting are presented in Table V.

## APPENDIX D: IMPACT OF QUANTUM CORRECTION

Molecular dynamics operates with classical laws of motion to evaluate the systems with a large number of degrees of freedom. Thus, quantum phenomena are naturally excluded from the consideration in this case. One of the commonly used approaches for taken them into account is based on the MD temperature rescaling to the temperature which includes quantum phenomena.<sup>73</sup> In this case, thermal conductivity may be corrected as follows:<sup>74</sup>

$$\kappa_{qc} = \kappa_{MD} \cdot \frac{dT_{MD}}{dT}, \quad (\text{D1})$$

where  $\kappa_{qc}$  is the quantum corrected thermal conductivity,  $\kappa_{MD}$  is the thermal conductivity evaluated with MD,  $T$  is the temperature, and  $T_{MD}$  is the classical temperature, which can be calculated as follows:

$$T_{MD} = \frac{T^2}{T_D} \cdot \int_0^{\frac{T_D}{T}} \frac{x dx}{\exp(x) - 1} + \frac{T_D}{4}, \quad (\text{D2})$$

where  $T_D$  is the Debye temperature.

Figure 9 (left scale) demonstrates temperature dependence of the derivative  $\frac{dT_{MD}}{dT}$ . This derivative defines the ratio of quantum corrected thermal conductivity to the MD one [Eq. (D1)]. As one can see from the figure, the quantum corrected thermal conductivity is less than the MD one approximately 10% at 300 K. Close to the Debye temperature ( $T_D = 658$  K for silicon) the difference is

**TABLE V.** Parameters of fitting for phonon lifetime.

	$A$ ( $s^{-1-\chi} K^{-\xi}$ )	$\xi$ (units)	$\chi$ (units)	$B$ (K)
Compressed	$1.523\,21 \cdot 10^{-14}$	1.604 16	1.085 86	0
Unstrained	$1.735\,48 \cdot 10^{-16}$	1.761 49	1.037 46	0
Tensed	$2.879\,35 \cdot 10^{-18}$	1.913 05	0.974 069	0

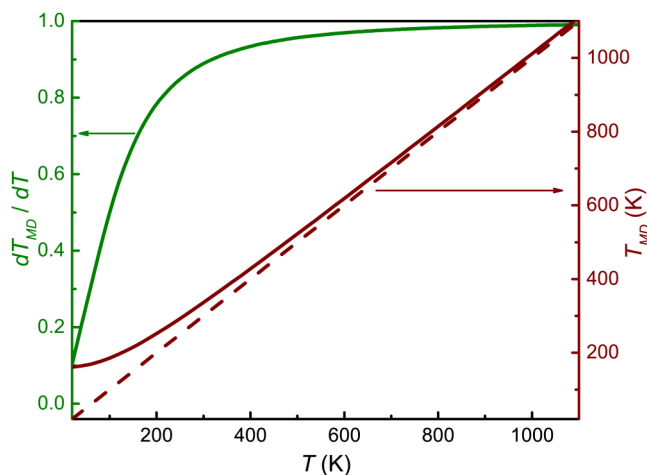


**FIG. 9.** Dependence of  $dT_{MD}/dT$  (left scale) and  $T_{MD}$  (right scale) on the corrected temperature. For comparison with the dotted line, the dependence  $T(T)$  for the right scale is presented.

less than 3%, and only after 1000 K, the value of the derivative is close to one. Thus, the impact of the quantum phenomena is significant for the temperatures less than  $T_D$ .

On the right scale of Fig. 9, we presented dependence of the MD temperature on the quantum corrected one. We presented the line which corresponds to the case  $T(T)$  with the dotted line.

The dependence of the quantum corrected in such a way thermal conductivity is presented in Fig. 10. In the correction, we neglected the change in the Debye temperature in the strained silicon. One can see that we achieve an excellent agreement of MD

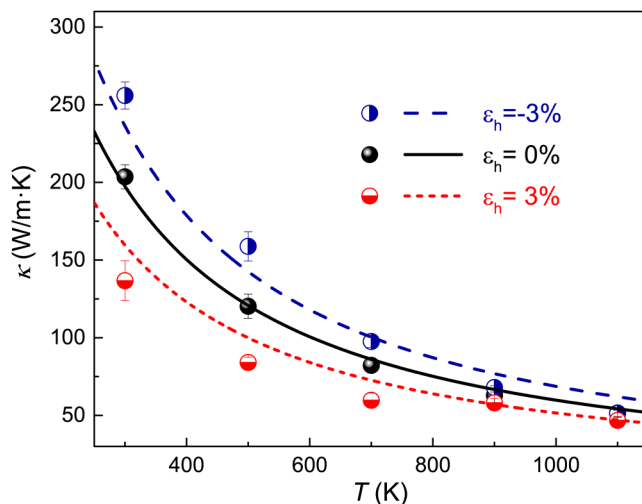


**FIG. 10.** Strain-dependent quantum corrected thermal conductivity of silicon between 300 and 1100 K for the Tersoff III potential.

data with the analytical approach. Nevertheless, the analytic model overestimates MD data for compressed silicon and underestimates for tensile one in the low temperature range. Such mismatches can be partially overcome with the correction of the Debye temperature, which arise mainly with slightly increasing sound velocity (see Fig. 1) in compressed silicon and decreasing in tensile one.

Finally, we should note that the use of the quantum correction in the presented above form is only illustrative, and thermal conductivity could not be fully corrected, see, for example, the results of quantum and classical lattice dynamics simulations presented by Turney *et al.*<sup>71</sup> Therefore, we decided to leave the part with the quantum correction only in the Appendix. Nevertheless, the presented results can be important for the understanding of mismatches of the kinetic theory analytic approach and MD data without quantum correction.

## REFERENCES

- <sup>1</sup>S. Volz, J. Ordóñez-Miranda, A. Shchepetov, M. Prunnila, J. Ahopelto, T. Pezeril, G. Vaudel, V. Gusev, P. Ruello, E. M. Weig, M. Schubert, M. Hettich, M. Grossman, T. Dekorsy, F. Alzina, B. Graczykowski, E. Chavez-Angel, J. Sebastian Reparaz, M. R. Wagner, C. M. Sotomayor-Torres, S. Xiong, S. Neogi, and D. Donadio, "Nanophononics: State of the art and perspectives," *Eur. Phys. J. B* **89**, 15 (2016).
- <sup>2</sup>D. G. Cahill, W. K. Ford, K. E. Goodson, G. D. Mahan, A. Majumdar, H. J. Maris, R. Merlin, and S. R. Phillpot, "Nanoscale thermal transport," *J. Appl. Phys.* **93**, 793–818 (2003).
- <sup>3</sup>D. G. Cahill, P. V. Braun, G. Chen, D. R. Clarke, S. Fan, K. E. Goodson, P. Keblinski, W. P. King, G. D. Mahan, A. Majumdar, H. J. Maris, S. R. Phillpot, E. Pop, and L. Shi, "Nanoscale thermal transport. II. 2003–2012," *Appl. Phys. Rev.* **1**, 011305 (2014).
- <sup>4</sup>*Nanostructured Semiconductors: Amorphization and Thermal Properties*, edited by K. Termentzidis (Pan Stanford, New York, 2017).
- <sup>5</sup>J. Zi, K. Zhang, and X. Xie, "Phonon spectra of strained Si and Ge," *Phys. Rev. B* **45**, 9447–9450 (1992).
- <sup>6</sup>Z. Sui and I. P. Herman, "Effect of strain on phonons in Si, Ge, and Si/Ge heterostructures," *Phys. Rev. B* **48**, 17938–17953 (1993).
- <sup>7</sup>S. Andersson and G. Backstrom, "The thermal conductivity and heat capacity of single-crystal Si under hydrostatic pressure," *J. Phys. C Solid State Phys.* **21**, 3727–3735 (1988).
- <sup>8</sup>A. F. Goncharov, M. Wong, D. Allen Dalton, J. G. O. Ojwang, V. V. Struzhkin, Z. Konopkova, and P. Lazor, "Thermal conductivity of argon at high pressures and high temperatures," *J. Appl. Phys.* **111**, 112609 (2012).
- <sup>9</sup>K. F. Murphy, B. Piccione, M. B. Zanjani, J. R. Lukes, and D. S. Gianola, "Strain- and defect-mediated thermal conductivity in silicon nanowires," *Nano Lett.* **14**, 3785–3792 (2014).
- <sup>10</sup>S. Bhowmick and V. B. Shenoy, "Effect of strain on the thermal conductivity of solids," *J. Chem. Phys.* **125**, 164513 (2006).
- <sup>11</sup>Y. Xu and G. Li, "Strain effect analysis on phonon thermal conductivity of two-dimensional nanocomposites," *J. Appl. Phys.* **106**, 114302 (2009).
- <sup>12</sup>K. D. Parrish, A. Jain, J. M. Larkin, W. A. Saidi, and A. J. H. McGaughey, "Origins of thermal conductivity changes in strained crystals," *Phys. Rev. B* **90**, 235201 (2014).
- <sup>13</sup>R. G. Ross, P. Andersson, B. Sundqvist, and G. Backstrom, "Thermal conductivity of solids and liquids under pressure," *Rep. Prog. Phys.* **47**, 1347–1402 (1984).
- <sup>14</sup>R. C. Picu, T. Borca-Tasciuc, and M. C. Pavel, "Strain and size effects on heat transport in nanostructures," *J. Appl. Phys.* **93**, 3535–3539 (2003).
- <sup>15</sup>X. Li, K. Maute, M. L. Dunn, and R. Yang, "Strain effects on the thermal conductivity of nanostructures," *Phys. Rev. B* **81**, 245318 (2010).

- <sup>16</sup>O. Marty, T. Nychyporuk, J. de la Torre, V. Lysenko, G. Bremond, and D. Barbier, "Straining of monocrystalline silicon thin films with the use of porous silicon as stress generating nanomaterial," *Appl. Phys. Lett.* **88**, 101909 (2006).
- <sup>17</sup>M. Isaiev, K. Voitenko, V. Doroshchuk, D. Andrusenko, A. Kuzmich, A. Skryshevskii, V. Lysenko, and R. Burbelo, "Thermal elasticity stresses study in composite system 'porous silicon—liquid'," *Phys. Procedia* **70**, 586–589 (2015).
- <sup>18</sup>V. Neimash, P. Shepelyavyi, G. Dovbeshko, A. O. Goushcha, M. Isaiev, V. Melnyk, O. Didukh, and A. Kuzmich, "Nanocrystals growth control during laser annealing of Sn:( $\alpha$ -Si) composites," *J. Nanomater.* **2016**, 7920238 (2016).
- <sup>19</sup>D. Fan, H. Sigg, R. Spolenak, and Y. Ekinici, "Strain and thermal conductivity in ultrathin suspended silicon nanowires," *Phys. Rev. B* **96**, 115307 (2017).
- <sup>20</sup>P. J. Newby, B. Canut, J.-M. Bluet, S. Gomés, M. Isaiev, R. Burbelo, K. Termentzidis, P. Chantrenne, L. G. Fréchette, and V. Lysenko, "Amorphization and reduction of thermal conductivity in porous silicon by irradiation with swift heavy ions," *J. Appl. Phys.* **114**, 014903 (2013).
- <sup>21</sup>N. D. Orekhov and V. V. Stegailov, "Swift heavy ion track formation in nanoporous Si: Wave packet molecular dynamics study," *J. Phys. Conf. Ser.* **946**, 012026 (2018).
- <sup>22</sup>O. Korotchenkov, A. Nadtochiy, V. Kuryliuk, C.-C. Wang, P.-W. Li, and A. Cantarero, "Thermoelectric energy conversion in layered structures with strained Ge quantum dots grown on Si surfaces," *Eur. Phys. J. B* **87**, 64 (2014).
- <sup>23</sup>V. Kuryliuk, A. Nadtochiy, O. Korotchenkov, C.-C. Wang, and P.-W. Li, "A model for predicting the thermal conductivity of SiO<sub>2</sub>–Ge nanoparticle composites," *Phys. Chem. Chem. Phys.* **17**, 13429–13441 (2015).
- <sup>24</sup>D. Midtvedt, A. Isacson, and A. Croy, "Nonlinear phononics using atomically thin membranes," *Nat. Commun.* **5**, 4838 (2014).
- <sup>25</sup>Y. Ni, S. Xiong, S. Volz, and T. Dumitrică, "Thermal transport along the dislocation line in silicon carbide," *Phys. Rev. Lett.* **113**, 124301 (2014).
- <sup>26</sup>J. Al-Ghalith, Y. Ni, and T. Dumitrică, "Nanowires with dislocations for ultra-low lattice thermal conductivity," *Phys. Chem. Chem. Phys.* **18**, 9888–9892 (2016).
- <sup>27</sup>K. Termentzidis, M. Isaiev, A. Salnikova, I. Belabbas, D. Lacroix, and J. Kioseoglou, "Impact of screw and edge dislocations on the thermal conductivity of individual nanowires and bulk GaN: A molecular dynamics study," *Phys. Chem. Chem. Phys.* **20**, 5159–5172 (2018).
- <sup>28</sup>T. Wang, J. Carrete, A. van Rooyeghem, N. Mingo, and G. K. H. Madsen, "Ab initio phonon scattering by dislocations," *Phys. Rev. B* **95**, 245304 (2017).
- <sup>29</sup>R. Yang, G. Chen, and M. S. Dresselhaus, "Thermal conductivity modeling of core-shell and tubular nanowires," *Nano Lett.* **5**, 1111–1115 (2005).
- <sup>30</sup>M. Isaiev, S. Tutashkonko, V. Jean, K. Termentzidis, T. Nychyporuk, D. Andrusenko, O. Marty, R. M. Burbelo, D. Lacroix, and V. Lysenko, "Thermal conductivity of meso-porous germanium," *Appl. Phys. Lett.* **105**, 031912 (2014).
- <sup>31</sup>J. Munguia, G. Bremond, J. de la Torre, and J.-M. Bluet, "Photoluminescence study of an ultrathin strained silicon on insulator layer," *Appl. Phys. Lett.* **90**, 042110 (2007).
- <sup>32</sup>J. Mansir, P. Conti, Z. Zeng, J. J. Pla, P. Bertet, M. W. Swift, C. G. Van de Walle, M. L. W. Thewalt, B. Sklenard, Y. M. Niquet, and J. J. L. Morton, "Linear hyperfine tuning of donor spins in silicon using hydrostatic strain," *Phys. Rev. Lett.* **120**, 167701 (2018).
- <sup>33</sup>M. Usman, H. Huebl, A. R. Stegner, C. D. Hill, M. S. Brandt, and L. C. L. Hollenberg, "Measurements and atomistic theory of electron  $g$ -factor anisotropy for phosphorus donors in strained silicon," *Phys. Rev. B* **98**, 035432 (2018).
- <sup>34</sup>F. H. Stillinger and T. A. Weber, "Computer simulation of local order in condensed phases of silicon," *Phys. Rev. B* **31**, 5262–5271 (1985).
- <sup>35</sup>J. Tersoff, "New empirical approach for the structure and energy of covalent systems," *Phys. Rev. B* **37**, 6991–7000 (1988).
- <sup>36</sup>J. A. F. Justo, M. Z. Bazant, E. Kaxiras, V. V. Bulatov, and S. Yip, "Interatomic potential for silicon defects and disordered phases," *Phys. Rev. B* **58**, 2539–2550 (1998).
- <sup>37</sup>M. I. Baskes, J. S. Nelson, and A. F. Wright, "Semiempirical modified embedded-atom potentials for silicon and germanium," *Phys. Rev. B* **40**, 6085–6100 (1989).
- <sup>38</sup>J. Tersoff, "Empirical interatomic potential for silicon with improved elastic properties," *Phys. Rev. B* **38**, 9902–9905 (1988).
- <sup>39</sup>J. Tersoff, "Modeling solid-state chemistry: Interatomic potentials for multi-component systems," *Phys. Rev. B* **39**, 5566–5568 (1989).
- <sup>40</sup>J. Tersoff, "Erratum: Modeling solid-state chemistry: Interatomic potentials for multicomponent systems," *Phys. Rev. B* **41**, 3248–3248 (1990).
- <sup>41</sup>B.-J. Lee and M. I. Baskes, "Second nearest-neighbor modified embedded-atom-method potential," *Phys. Rev. B* **62**, 8564–8567 (2000).
- <sup>42</sup>B.-J. Lee, M. Baskes, H. Kim, and Y. Koo Cho, "Second nearest-neighbor modified embedded atom method potentials for bcc transition metals," *Phys. Rev. B* **64**, 184102 (2001).
- <sup>43</sup>C. Abs da Cruz, K. Termentzidis, P. Chantrenne, and X. Kleber, "Molecular dynamics simulations for the prediction of thermal conductivity of bulk silicon and silicon nanowires: Influence of interatomic potentials and boundary conditions," *J. Appl. Phys.* **110**, 034309 (2011).
- <sup>44</sup>P. C. Howell, "Comparison of molecular dynamics methods and interatomic potentials for calculating the thermal conductivity of silicon," *J. Chem. Phys.* **137**, 224111 (2012).
- <sup>45</sup>M. S. El-Genk, K. Talaat, and B. J. Cowen, "Thermal conductivity of silicon using reverse non-equilibrium molecular dynamics," *J. Appl. Phys.* **123**, 205104 (2018).
- <sup>46</sup>P. Chantrenne, J. L. Barrat, X. Blase, and J. D. Gale, "An analytical model for the thermal conductivity of silicon nanostructures," *J. Appl. Phys.* **97**, 104318 (2005).
- <sup>47</sup>D. P. Sellan, E. S. Landry, J. E. Turney, A. J. H. McGaughey, and C. H. Amon, "Size effects in molecular dynamics thermal conductivity predictions," *Phys. Rev. B* **81**, 214305 (2010).
- <sup>48</sup>Z. Wang and X. Ruan, "On the domain size effect of thermal conductivities from equilibrium and nonequilibrium molecular dynamics simulations," *J. Appl. Phys.* **121**, 044301 (2017).
- <sup>49</sup>M. A. Hopcroft, W. D. Nix, and T. W. Kenny, "What is the Young's modulus of silicon?," *J. Microelectromech. Syst.* **19**, 229–238 (2010).
- <sup>50</sup>See [http://www.matprop.ru/Si\\_mechanic](http://www.matprop.ru/Si_mechanic) for more information about elastic properties of crystalline silicon.
- <sup>51</sup>K. Mizushima, S. Yip, and E. Kaxiras, "Ideal crystal stability and pressure-induced phase transition in silicon," *Phys. Rev. B* **50**, 14952–14959 (1994).
- <sup>52</sup>C. C. Yang, J. C. Li, and Q. Jiang, "Temperature-pressure phase diagram of silicon determined by Clapeyron equation," *Solid State Commun.* **129**, 437–441 (2004).
- <sup>53</sup>A. J. H. McGaughey and M. Kaviani, "Quantitative validation of the Boltzmann transport equation phonon thermal conductivity model under the single-mode relaxation time approximation," *Phys. Rev. B* **69**, 094303 (2004); e-print [arXiv:1412.6057](https://arxiv.org/abs/1412.6057).
- <sup>54</sup>L. T. Kong, G. Bartels, C. Campaña, C. Denniston, and M. H. Müser, "Implementation of Green's function molecular dynamics: An extension to LAMMPS," *Comput. Phys. Commun.* **180**, 1004–1010 (2009).
- <sup>55</sup>L. T. Kong, "Phonon dispersion measured directly from molecular dynamics simulations," *Comput. Phys. Commun.* **182**, 2201–2207 (2011).
- <sup>56</sup>D. Dickel and M. S. Daw, "Improved calculation of vibrational mode lifetimes in anharmonic solids. Part I: Theory," *Comput. Mater. Sci.* **47**, 698–704 (2010).
- <sup>57</sup>D. Dickel and M. S. Daw, "Improved calculation of vibrational mode lifetimes in anharmonic solids. Part II: Numerical results," *Comput. Mater. Sci.* **49**, 445–449 (2010).
- <sup>58</sup>Y. Gao, D. Dickel, D. Harrison, and M. S. Daw, "Improved calculation of vibrational mode lifetimes in anharmonic solids. Part III: Extension to fourth moment," *Comput. Mater. Sci.* **89**, 12–18 (2014).
- <sup>59</sup>Y. Gao, H. Wang, and M. S. Daw, "Calculations of lattice vibrational mode lifetimes using jazz: A python wrapper for LAMMPS," *Model. Simul. Mater. Sci. Eng.* **23**, 045002 (2015).

- <sup>60</sup>See <https://sourceforge.net/projects/jazzforlammps/> for more information about Jazz, a new python wrapper for LAMMPS.
- <sup>61</sup>C. J. Glassbrenner and G. A. Slack, "Thermal conductivity of silicon and germanium from 3 K to the melting point," *Phys. Rev.* **134**, A1058–A1069 (1964).
- <sup>62</sup>A. V. Inyushkin, A. N. Taldenkov, J. W. Ager, E. E. Haller, H. Riemann, N. V. Abrosimov, H.-J. Pohl, and P. Becker, "Ultra-high thermal conductivity of isotopically enriched silicon," *J. Appl. Phys.* **123**, 095112 (2018).
- <sup>63</sup>J.-H. Lee, J. C. Grossman, J. Reed, and G. Galli, "Lattice thermal conductivity of nanoporous Si: Molecular dynamics study," *Appl. Phys. Lett.* **91**, 223110 (2007).
- <sup>64</sup>Z. Yang, R. Feng, F. Su, D. Hu, and X. Ma, "Isotope and strain effects on thermal conductivity of silicon thin film," *Physica E* **64**, 204–210 (2014).
- <sup>65</sup>M. G. Shahraki and Z. Zeinali, "Effects of vacancy defects and axial strain on thermal conductivity of silicon nanowires: A reverse nonequilibrium molecular dynamics simulation," *J. Phys. Chem. Solids* **85**, 233–238 (2015).
- <sup>66</sup>B. A. Weinstein and G. J. Piermarini, "Raman scattering and phonon dispersion in Si and gap at very high pressure," *Phys. Rev. B* **12**, 1172–1186 (1975).
- <sup>67</sup>K. Esfarjani, G. Chen, and H. T. Stokes, "Heat transport in silicon from first-principles calculations," *Phys. Rev. B* **84**, 085204 (2011).
- <sup>68</sup>J. M. Larkin and A. J. H. McGaughey, "Predicting alloy vibrational mode properties using lattice dynamics calculations, molecular dynamics simulations, and the virtual crystal approximation," *J. Appl. Phys.* **114**, 023507 (2013).
- <sup>69</sup>D. S. Kim, H. L. Smith, J. L. Niedziela, C. W. Li, D. L. Abernathy, and B. Fultz, "Phonon anharmonicity in silicon from 100 to 1500 K," *Phys. Rev. B* **91**, 014307 (2015).
- <sup>70</sup>C. Flensburg and R. F. Stewart, "Lattice dynamical Debye-Waller factor for silicon," *Phys. Rev. B* **60**, 284–291 (1999).
- <sup>71</sup>J. E. Turney, A. J. H. McGaughey, and C. H. Amon, "Assessing the applicability of quantum corrections to classical thermal conductivity predictions," *Phys. Rev. B* **79**, 224305 (2009).
- <sup>72</sup>B.-J. Lee, "A modified embedded atom method interatomic potential for silicon," *Calphad* **31**, 95–104 (2007).
- <sup>73</sup>A. Soleimani, H. Araghi, Z. Zabihi, and A. Alibakhshi, "A comparative study of molecular dynamics simulation methods for evaluation of the thermal conductivity and phonon transport in Si nanowires," *Comput. Mater. Sci.* **142**, 346–354 (2018).
- <sup>74</sup>Y. H. Lee, R. Biswas, C. M. Soukoulis, C. Z. Wang, C. T. Chan, and K. M. Ho, "Molecular-dynamics simulation of thermal conductivity in amorphous silicon," *Phys. Rev. B* **43**, 6573–6580 (1991).
- <sup>75</sup>S. Plimpton, "Fast Parallel Algorithms for Short-Range Molecular Dynamics," *J. Comp. Phys.* **117**, 1–19 (1995).